

Electronic modulation of metal-support interactions improves polypropylene hydrogenolysis over ruthenium catalysts

Received: 6 April 2022

Accepted: 24 August 2022

Published online: 03 September 2022

Check for updates

Pavel A. Kots¹, Tianjun Xie¹, Brandon C. Vance^{1,2}, Caitlin M. Quinn³, Matheus Dorneles de Mello⁴, J. Anibal Boscoboinik⁴, Cong Wang¹, Pawan Kumar⁵, Eric A. Stach⁵, Nebojsa S. Marinkovic⁶, Lu Ma⁷, Steven N. Ehrlich⁷ & Dionisios G. Vlachos^{1,2} ✉

Ruthenium (Ru) is the one of the most promising catalysts for polyolefin hydrogenolysis. Its performance varies widely with the support, but the reasons remain unknown. Here, we introduce a simple synthetic strategy (using ammonia as a modulator) to tune metal-support interactions and apply it to Ru deposited on titania (TiO₂). We demonstrate that combining deuterium nuclear magnetic resonance spectroscopy with temperature variation and density functional theory can reveal the complex nature, binding strength, and H amount. H₂ activation occurs heterolytically, leading to a hydride on Ru, an H⁺ on the nearest oxygen, and a partially positively charged Ru. This leads to partial reduction of TiO₂ and high coverages of H for spillover, showcasing a threefold increase in hydrogenolysis rates. This result points to the key role of the surface hydrogen coverage in improving hydrogenolysis catalyst performance.

Plastic waste represents a significant threat to the environment due to its leakage into the oceans and soil. Plastic consumption increased drastically during the recent pandemic¹, triggering a soaring expansion of incineration, causing extensive CO₂ emissions², and landfilling of consumer packaging materials, foams, films, and personal protection equipment³. Polypropylene (PP) is a large-volume polymer frequently used in packaging, fabrics, and textiles, including face masks. Mechanical recycling fails to deal with mixed PP waste streams since composites usually contain pigments, dyes, antioxidants, and plasticizers, leading to an inferior product. PureCycle⁴ has demonstrated that solvent extraction can provide consumer-grade PP, but solvent use increases cost and complexity. A possible approach to extend the life cycle is the catalytic conversion of PP waste under solvent-free conditions.

Hydrogenolysis is a low-energy valorization route of PP and polyethylene (PE)⁵, producing liquid products, including lubricant base oil⁶. Ru and Pt nanoparticles on carbon or oxide supports have been the hydrogenolysis catalysts of choice^{7–11}. Ru, in particular, is more active than Pt but forms copious amounts of methane, and reaction times are long. Its performance varies widely with the support, but the reasons remain unclear^{7,10–14}. For example, over Ru/ZrO₂, the strong PE binding leads to the over-cracking of the reaction intermediates to methane¹⁵. On Ru/WO_x/ZrO₂, on the other hand, hydrogen spillover from Ru stores hydrogen in reducible surface polytungstate domains, thus effectively removing reaction intermediates and suppressing methane formation. Recent work on Ru deposited on redox-active CeO₂ support showed 83% liquid yield. Controlling hydrogen availability on the catalyst and polyolefin

¹Center for Plastics Innovation, University of Delaware, 221 Academy St., Newark, DE 19716, USA. ²Department of Chemical and Biomolecular Engineering, University of Delaware, 150 Academy St., Newark, DE 19716, USA. ³Department of Chemistry and Biochemistry, University of Delaware, Newark, DE 19716, USA. ⁴Center for Functional Nanomaterials, Brookhaven National Laboratory, 735 Brookhaven Ave, Upton, NY 11973, USA. ⁵Department of Materials Science and Engineering, University of Pennsylvania, Philadelphia, PA 19104, USA. ⁶Department of Chemical Engineering, Columbia University, 500W 120th St., New York, NY 10027, USA. ⁷National Synchrotron Light Source II, Brookhaven National Laboratory, Upton, NY 11973, USA. ✉ e-mail: vlachos@udel.edu

binding may effectively control the chemistry, but ways to achieve this are lacking.

Here, we introduce a systematic approach to tune the reducibility of the TiO₂ support and the metal-support interactions (MSI). Formation of TiO_x overlayer reported initially in ref. 16 is known to poison the metal surface and inhibit hydrogen chemisorption. For the Ru/TiO₂ catalyst, the MSI enhanced by the lattice matching between RuO_x and rutile TiO₂ leads to higher catalytic activity in CO₂ hydrogenation¹⁷. We perform extensive characterization and correlate the electronic properties and hydrogen storage to catalytic performance in PP hydrogenolysis. We show that extensive reduction of TiO₂ via hydrogen spillover from Ru modifies the hydrogen storage capacity of the Ru nanoparticles. This boosts the hydrogenolysis activity and reduces the liquid molecular weight and the reaction time.

Results

Ru/TiO₂ catalyst characterization

We changed the pH in the Ru deposition step, using aqueous NH₃, to modify the catalyst (catalysts are labeled as Ru/TiO₂-x, where x indicates the synthesis pH) while ensuring similar Ru loadings (~3 wt%), surface areas (100 m²/g) (Table 1), and pore volume. According to XPS quantitative analysis, all samples have similar surface Ru/Ti atomic ratios consistent with the same Ru loadings. XRD patterns (Supplementary Fig. 1) show relatively broad reflections of the TiO₂ anatase support with no sign of crystalline Ru. Ex situ UV-Vis spectra reveal comparable bandgap energies, typical of pure anatase TiO₂ (Table 1). All samples contain predominantly 1.4–1.6 nm Ru nanoparticles evenly distributed on TiO₂ (STEM images in Fig. 1a, b and particle size distribution in Supplementary Fig. 2). TiO₂ consists of elongated cylindrical, highly crystalline particles of 35–40 nm length and ~10 nm diameter. In situ Ru K-edge XANES spectra (Supplementary Fig. 3) after pre-reduction with H₂ at 250 °C indicate metallic Ru⁰ and EXAFS spectral analysis (Table 1, Fig. 1c, Supplementary Fig. 3, Supplementary Table 1) show a coordination number of ~8.5, consistent with the STEM images.

TGA results (Supplementary Fig. 4) show that ~10 mmol/g_{TiO₂} of NH₃ is retained after impregnation, an order of magnitude higher than Ti⁴⁺ on the surface¹⁸. NH₃ desorbs in H₂/He at ~250 °C, indicating strong interaction with the catalyst. NH₃ can reduce and modify the TiO₂ surface after high-temperature treatment^{19,20}. Based on DRIFTS spectra (Supplementary Fig. 5) of Ru/TiO₂-8 directly after impregnation and drying and before the reduction in H₂, ammonia is adsorbed in several modes. Two possible mechanisms are proposed to explain the NH₃ role during sample pre-reduction (Supplementary Figs. 6–8). XPS analysis shows no signs of N-doping of TiO₂ after reduction.

To investigate the modification of the Lewis acidity, we used FTIR of adsorbed CO at -196 °C (Fig. 1d, e). At high CO pressure, Lewis acid

site bands appear at 2206 and 2179 cm⁻¹ due to highly electrophilic four-coordinated Ti⁴⁺(O₄) sites on the particle edges and the less acidic five-coordinated Ti⁴⁺(O₅) sites on the 101 crystal planes, respectively²¹. The concentration of Ti⁴⁺(O₄) sites is similar in both samples. The intensity of both bands decreases with evacuation time, but the 2206 cm⁻¹ band is reduced more slowly. Ru/TiO₂-8 retains some CO on both sites even after prolonged evacuation, whereas Ru/TiO₂-1 only marginally on the stronger Ti⁴⁺(O₄) sites (Fig. 1e), indicating stronger binding and Lewis acidity on the former (Supplementary Fig. 9). DRIFTS demonstrates a smaller density of surface Ti-OH groups on the Ru/TiO₂-8 and Ru/TiO₂-12 than on Ru/TiO₂-1 (Supplementary Fig. 10). Partial dehydroxylation enhances the Lewis acidity of Ti⁴⁺ sites due to the redistribution of the electron density on the surface²².

In addition to Ti⁴⁺-CO adducts, FTIR spectra show that Ru particles get partially oxidized by CO forming multiple Ru^{m+}(CO)_m (m = 1–4) carbonyls with ν(CO) vibration at 2136, 2106, 2084, and 2055 cm⁻¹ (Supplementary Fig. 11)²³. Due to the low-temperature CO dissociation, clusters of Ru⁺ and Ru⁰ species form. The stronger interaction of TiO₂ and Ru and the TiO_x peripheral layer shifts the broad ν(CO) band to lower wavenumbers²⁴ (from 2077 to 2059 cm⁻¹, Fig. 1d), epitomizing a proximal MSI in the Ru/TiO₂-8 catalyst.

Hydrogen binding on Ru/TiO₂

H₂ temperature-programmed desorption (TPD) (Supplementary Fig. 12) indicates a similar amount of strongly chemisorbed hydrogen on the Ru (low-temperature peak at 160 °C)²⁵ and TiO₂ (high-temperature shoulder at 250–300 °C)²⁶. Temperature-programmed reduction (TPR) in H₂ flow shows a spike in hydrogen adsorption at 80–90 °C, due to binding on Ru, and a broad peak starting at ca. 250 °C, due to partial TiO₂ reduction (Supplementary Fig. 13). Interestingly, Ru/TiO₂-8 and Ru/TiO₂-12 show more pronounced hydrogen uptakes at 150–200 °C than Ru/TiO₂-1. Hydrogen pulse chemisorption at 35 °C (Table 1) shows that Ru/TiO₂ samples have different hydrogen uptakes. During an experiment, hydrogen can spillover to the TiO₂ support obscuring the real Ru dispersion values. Thus the total H₂ uptake inferred from pulse chemisorption depends on the spillover capacity of TiO₂, rendering accurate quantification of the exposed Ru surface area impossible with the available methods. Also, the pre-treatment temperature before pulse chemisorption (300 °C) is insufficient to remove all chemisorbed hydrogen from the sample. Thus, apparent uptakes may be higher for catalysts with weaker chemisorption.

To decouple Ru from support contributions to the hydrogen binding and activation, we used ²H MAS NMR of chemisorbed D₂ (Fig. 2). Chemisorption of ²H on Ru clusters is accompanied by quadrupole interactions with the surrounding electric field gradient (EFG), leading to characteristic sidebands in the NMR spectra. Spectra contours depend on the quadrupole coupling constant (Q_{cc}), a function of the largest EFG component (V_{zz}), and the asymmetry parameter η, defined as (V_{xx} - V_{yy})/V_{zz}. One can obtain the EFG parameters, sensitive to the deuteron local surroundings and the binding type^{27,28}.

Figure 2a shows a complex line shape after sample reduction followed by saturation with 1 torr of D₂. Deconvolution yields several components (Fig. 2b, c; high-resolution data at 10 kHz shown in Supplementary Fig. 14). The first component (Q_{cc}-123–130 kHz/η-0.7–1.0) corresponds to Ti-OD formed by deuterium spillover, confirmed by measuring a D₂O-treated pure TiO₂ sample (Fig. 2f, Supplementary Fig. 15, Supplementary Table 2). Also, a simple H/D isotope exchange leads to the formation of Ti-OD groups²⁹, and their presence in the spectra is not a fingerprint of spillover.

The latter peak has a symmetric EFG (η-0.1) and low Q_{cc} of ca. 70 kHz, distinctly different from the Ti-OD signal (Fig. 2e, Supplementary Table 3), and consistent with Ru_n-D hydrides²⁷. The second component corresponds to deuterons bonded to Ru in atop conformation (see parameters in Supplementary Tables 3 and 4),

Table 1 | Ru/TiO₂ catalyst characterization

Catalyst property	Ru-TiO ₂ -1	Ru-TiO ₂ -8	Ru-TiO ₂ -12
Ru loading, wt%	3.1	3.1	3.3
(Ru/Ti) _{bulk} ^a	0.025	0.025	0.027
(Ru/Ti) _{surf} ^b	0.19	0.20	0.22
d(Ru) _{TEM} , nm	1.4	1.2	1.4
H _{chem} , μmol/g ^c	270	180	140
D _H , % ^d	88	59	43
E _g , eV ^e	3.2	3.2	2.8
S _{BET} , m ² /g	100	90	95
V _p , cm ³ /g	0.35	0.33	0.33

^aMeasured by XRF.

^bMeasured by XPS.

^cChemisorbed hydrogen measured by pulse chemisorption.

^dApparent dispersion estimated from pulse chemisorption assuming H_{chem}/Ru_{surf} ratio 1.

^eOptical bandgap measured by UV-Vis spectroscopy.

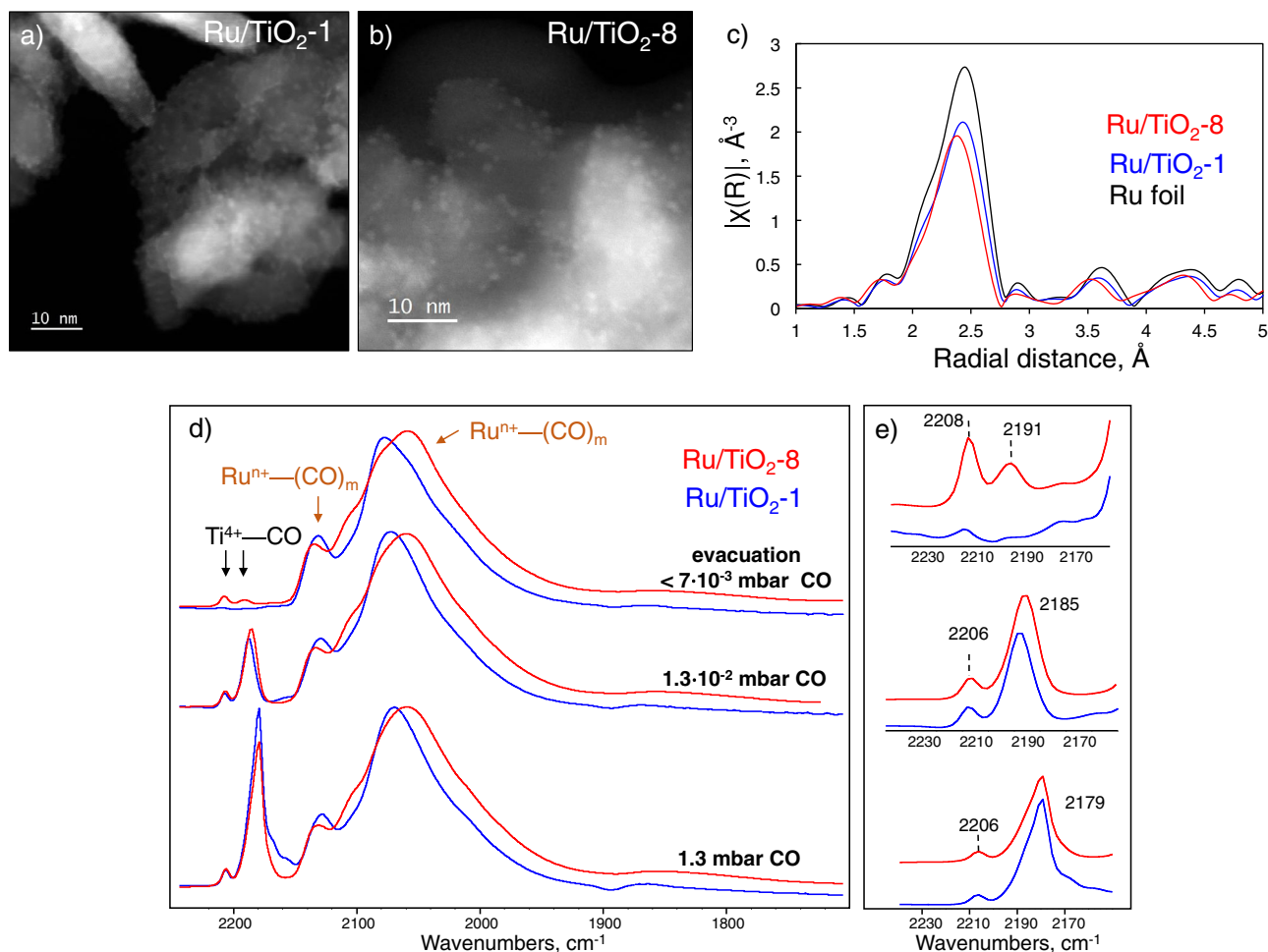


Fig. 1 | Catalyst characterization. **a, b** STEM images of Ru/TiO₂-1 and Ru/TiO₂-8, respectively; **c** EXAFS spectra of two samples and Ru foil standard; **d** FTIR of adsorbed CO at -296 °C at different CO pressures; **e** Zoom in of the 2240–2150 cm⁻¹ region.

confirmed using DFT calculations (Supplementary Fig. 16). Figure 2g shows an optimized structure of a Ru cluster on TiO₂ with a D atom, in good agreement with a previous report³⁰, underscoring the preferential formation of atop H instead of (Ru)₂-H bridging binding. The EFG parameters depend on the Ru particle size and the support. For an unsupported Ru₁₂ cluster, EFG is more symmetric, unlike the experimental data. Smaller or larger clusters than Ru₁₂ on TiO₂ provide a less adequate EFG. Thus, ²H NMR, combined with DFT, provides insights into MSI and particle size effects.

The third component gives a very broad single line with no sidebands (Fig. 2d) at a low resonance frequency (-4 to -4.4 kHz, or -53 to -57.3 ppm). These features are not standard for Ru_n-D hydrides, observed previously for free-standing Ru clusters²⁷. The negative chemical shift is similar to chemisorbed hydrogen on Ru particles on SiO₂ and TiO₂, inferred from static ¹H NMR^{31,32}. The deuteron interaction with the Ru conduction electrons leads to the so-called Knight shift responsible for the -53 ppm peak³³. On Ru/SiO₂, this peak stems from the overlap of different signals due to strongly and weakly chemisorbed hydrogen³¹. We exclude deuteron binding to an oxygen vacancy in TiO₂ because it would lead to resonances close to 0 kHz at -1.07 ppm³⁴ or -0.66 ppm and -0.78 ppm³⁵. Static ¹H NMR studies showed that the exact position and linewidth are highly affected by Na doping of a Ru/TiO₂ catalyst³⁶, i.e., this deuteron is sensitive to interactions with the support. In our case, direct interaction via Fermi contact between Ti³⁺ paramagnetic sites on the partially reduced TiO_x support can affect the position and intensity of this peak.

Sample evacuation at 100 °C leads to a significant reduction in the intensity of the -53.2 ppm peak and shifting to -45.8 ppm (lower Knight shift) (Supplementary Figs. 17, 18, Supplementary Table 5). Interestingly, the ratio of Ti-OD and Ru-D_{atop} groups remains constant, indicating comparable stability. Thus, the resonance at -53.2 ppm corresponds to the weakly bonded deuteron, not entirely captured in the TPD. Unlike the Ru-D_{atop} signal, these deuterons are trapped by the Ru's conduction electrons or some Ti³⁺ charged center of the support. Based on the thermal stability of the adsorbed deuterium studied by ²H MAS NMR and TPD, all three types of surface deuterons are stable at 25 °C and desorb only upon heating.

The ²H MAS NMR spectra reveal significant differences in the deuterons (Fig. 2h,i, Supplementary Fig. 19). The NH₃-treated samples have a much higher content of Ru-bonded deuterium than Ti-OD groups. Higher resolution 10 kHz MAS spectra (Fig. 2h, i) show that Ru-related peaks at 0.18 kHz (2.1 ppm) and -4.49 kHz (-58.0 ppm) over Ru/TiO₂-8 are more pronounced than on Ru/TiO₂-1. The data combined (Supplementary Table 6, 7) reveals that Ru/TiO₂-8 has a higher absolute amount of Ru-bonded deuterium. This was further supported by a direct comparison of relative distributions of different deuterons. Thus, NH₃-treated supports promote hydrogen binding to Ru clusters.

Dynamics of hydrogen-Ru/TiO₂ interactions

Hydrogen can partially reduce the TiO₂ support by hydrogen spillover (Fig. 3)²⁹, forming OH groups, and injecting electrons into TiO₂, creating Ti³⁺ sites as a new state in the bandgap (Fig. 3a)³⁷. Thermal excitation could also cause electron delocalization and populate the

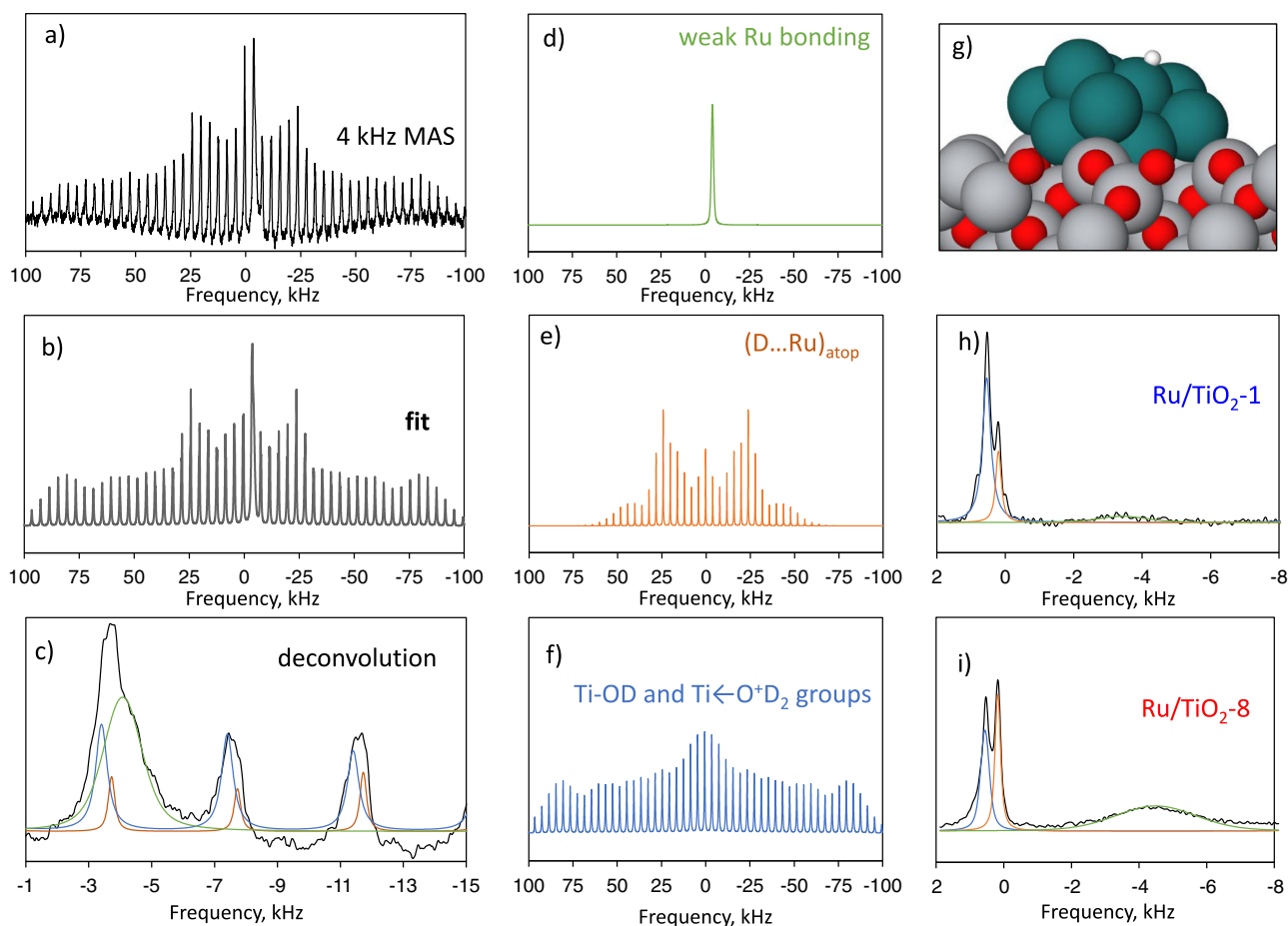


Fig. 2 | Hydrogen chemisorption on Ru/TiO₂. **a** Solid-state ²H MAS NMR spectra of Ru/TiO₂-8 measured at 4 kHz of spinning. **b** Fitting of experimental spectra. **c** Zoom in low-frequencies alongside three components used for fitting, resolved via deconvolution. **d–f** Deconvoluted signals of weakly bonded D on Ru (**d**), strongly bonded D on Ru in atop configuration, **e**, and Ti-OD and Ti←O⁺D₂ groups on TiO₂ (**f**). **g** DFT-deduced structure of atop bonded D on a Ru cluster. **h, i** Spectra at 10 kHz MAS for Ru/TiO₂-1 (**h**) and Ru/TiO₂-8 (**i**).

titanium conduction band (CB)³⁸. Specifically, hydrogen spillover creates a Ti³⁺ shallow trap, 0.1–0.2 eV below the CB edge, and a broadband in the FTIR spectra (Fig. 3c), frequently used to study spillover^{39,40}. Electrons residing in the CB produce a power-law type spectrum distinct from shallow traps.

On Ru/TiO₂-1, hydrogen binding leads primarily to shallow trap electrons (Fig. 3d). Due to the reversible spillover, this partial reduction is sensitive to temperature and hydrogen pressure (Supplementary Figs. 20, 21). A much broader background increase is seen on Ru/TiO₂-8 due to the additional partial CB filling (Fig. 3e, Supplementary Fig. 22). The Ti-OH groups give a slight negative peak of ν(OH) at 3665 cm⁻¹, and a new peak for δ(HOH) at 1614 cm⁻¹ emerges due to the recombinative dehydroxylation of vicinal Ti-OH groups into water. Water formation stimulates the population of CB electrons⁴¹. FTIR shows that Ru/TiO₂-1 is mainly reduced into localized Ti³⁺ states, whereas NH₃-treated samples produce delocalized CB electrons (Fig. 3f). Hydrogen spillover is activated only at sufficiently high H coverage on Ru particles³⁰, i.e., the low H coverage on the Ru/TiO₂-1 sample (detected by ²H NMR) does not promote spillover and TiO₂ reduction to the same extent.

In situ Raman spectroscopy at 200 °C in He and H₂/He flows (Fig. 3g, h) corroborates this result. The E_g(1) vibrational mode of TiO₂ anatase (−144 cm⁻¹) is sensitive to the concentration of electrons⁴². On Ru/TiO₂-1, the peak position is unaffected by hydrogen (Fig. 3g). In contrast, on Ru/TiO₂-8 it shifts by −3 cm⁻¹ due to forming CB electrons by hydrogen; shallow traps (Ti³⁺ states) do not contribute.

The extent of reduction and associated charge transfer were monitored using NAP-XPS. Upon introducing hydrogen at 200 °C to Ru/TiO₂-8, the Ti 2p_{3/2} peak (458.69 eV; Fig. 3i, Supplementary Fig. 23, Supplementary Table 8) and the main lattice oxygen peak in the O 1s region⁴³ (Fig. 3j) shift to lower binding energies by 0.15 eV due to modest support reduction. No shifts are evident on Ru/TiO₂-1, indicating low receptivity toward hydrogen. Since the penetration depth of NAP-XPS corresponds to 2–3 nm, the Ru 3d and Ti 2p signals are collected from the whole Ru nanoparticle volume and 1–2 atomic layers of the underlying TiO₂ support⁴⁴. Thus, changes in the XPS spectra reflect charge distribution and MSI, but are not sensitive to the formation of the narrow TiO_x peripheral layer observed in the FTIR of CO experiments (Fig. 1d).

The Ru 3d doublet overlaps with the C 1s signal caused by carbonaceous deposits on the initial TiO₂ (Fig. 3k). Ru/TiO₂-1 and Ru/TiO₂-8 have slightly different binding energy (BE): 279.70 and 280.12 eV, respectively (Supplementary Table 8). Such values are typical for small Ru particles on TiO₂⁴⁴. Upon exposure of Ru/TiO₂-1 to hydrogen at 200 °C, the BE of the Ru 3d_{5/2} peak increases by 0.12 eV; over Ru/TiO₂-8, it shifts by 0.61 eV, indicative of Ru^{δ+} species. H₂ activation at the Ru-TiO₂ interface leads to negatively charged H⁻ attached to the metal and H⁺ binding to the nearest oxygen atom (Fig. 3b)⁴⁵. This heterolytic hydrogen activation leads to a partial positive charge on Ru due to forming negatively charged hydrides (H⁻) (Fig. 3b). The direct charge transfer from Ru to TiO₂ CB leads to a partial reduction of TiO₂, as reported in CO₂ reduction⁴⁶. Ru^{δ+}-H⁻ pairs upon H₂ adsorption were

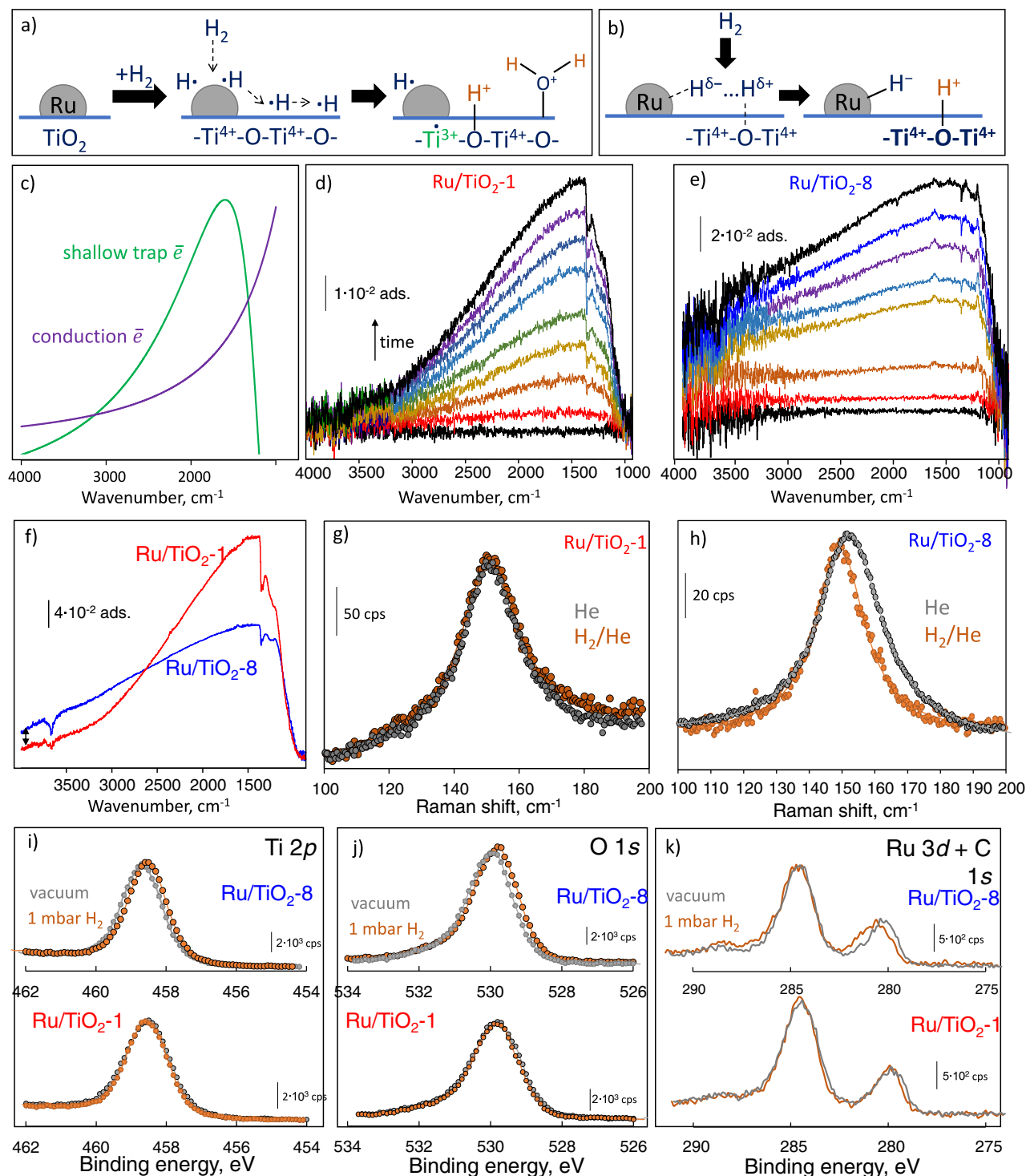


Fig. 3 | Hydrogen activation over Ru/TiO₂. **a** Hydrogen spillover schematic over Ru/TiO₂. **b** H₂ binding on the metal-support interface. **c** Theoretical IR spectra for free electrons in the TiO₂ conduction band and Ti³⁺ shallow trapped electrons. **d, e** Transmission FTIR transient spectra when switching from pure He to H₂/He flow at 200 °C on Ru/TiO₂-1 and Ru/TiO₂-8, respectively. **f** Steady-state FTIR

spectra for both samples at 250 °C and 0.14 bar H₂. **g, h** In situ Raman spectra for Ru/TiO₂-1 and Ru/TiO₂-8 at 200 °C in He and H₂/He flows, respectively (lines show Lorentzian curve fitting). **i–k** NAP-XPS of Ru/TiO₂ samples under high vacuum and 1 mbar H₂ pressure at 200 °C in T 2*p* (**i**), O 1*s* (**j**), and Ru 3*d* (**k**) regions.

also reported on Ru/carbon nanotubes⁴⁷. Ru on NH₃-treated supports allows spillover of H₂, forming delocalized electrons, reducing the support more extensively, and increasing the positive charge of Ru.

PP hydrogenolysis

PP hydrogenolysis data over the three Ru/TiO₂ samples with two polymer/catalyst weight ratios, 20 and 40, is shown in Fig. 4a–c and

Supplementary Figs. 22, 23. The liquid yield increases with time and reaches 74% (Ru/TiO₂-8) and 65–70% (Ru/TiO₂-12) at 6 h, compared to only 63% at much longer times of 20 h (Ru/TiO₂-1) reported earlier⁶. The conversion of the solid residue follows the same trend. The liquid product's weight-average molecular weight (*M_w*) (Fig. 4c, Supplementary Tables 9, 10) is lower over Ru/TiO₂-8 and Ru/TiO₂-12 than Ru/TiO₂-1.

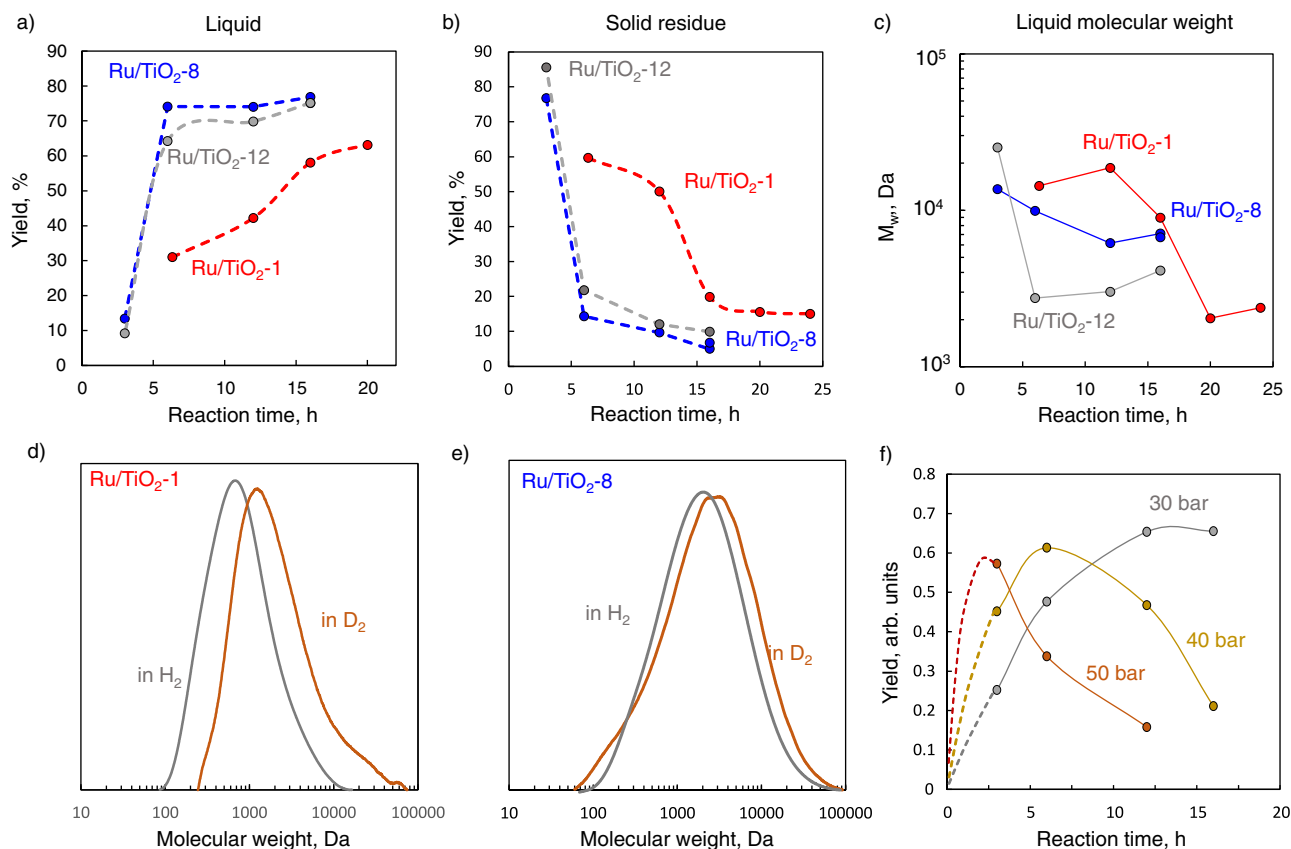


Fig. 4 | Ru/TiO₂ hydrogenolysis performance in PP deconstruction. a, b Yields of liquids (a) and solid residue (b) vs. time. **c** M_w of liquid vs. time. **d, e** Effect of substitution of H₂ with D₂ on liquid molecular weight distribution over Ru/TiO₂-1 (d) and Ru/TiO₂-8 (e) catalysts. **f** Effect of hydrogen pressure on liquid yield over Ru/TiO₂-1 (the dotted line extrapolates the data, using a simple A → B → C kinetic scheme). Conditions: 250 °C, 30 bar H₂, 2 g PP, 0.05 g catalyst (a, c) or 0.1 g catalyst (b, d–f) for a PP/catalyst ratio of 40 and 20, respectively.

PP conversion follows⁶ (i) an initial polymer consumption forming a “heavy” liquid; (ii) a decrease of the liquid M_w; and (iii) consumption of the liquid to light gases (~85% methane). When the M_w reaches a critical value, cascade hydrogenolysis to gas starts. Ru/TiO₂-8 and Ru/TiO₂-12 substantially increase the solid consumption and the liquid C–C bond hydrogenolysis compared to Ru/TiO₂-1, leading to lighter products (Fig. 4c, Supplementary Tables 9, 10).

All catalysts show similar methane formation up to ca. 10% at long reaction times due to excessive liquid hydrogenolysis (Supplementary Figs. 24, 25, Supplementary Table 11). To study liquid gasification in more detail, we performed experiments at a higher polymer to catalyst ratio of 20 (Fig. 4b). The liquid stability increases in the order: Ru/TiO₂-12 < Ru/TiO₂-8 < Ru/TiO₂-1 in line with the liquid M_w.

In the PE conversion over Ru/ZrO₂ and Ru/WO_x/ZrO₂, the hydrogen availability on Ru was crucial in controlling the hydrogenolysis selectivity to liquids vs. light gases¹⁵. A high intrinsic H coverage favors liquid products. Conversely, a low H coverage promotes a sequential cascade of C–C rupture to methane.

We hypothesize that the performance differences among catalysts stem from the H coverage on Ru. We perform experiments of varying H₂ pressure (Fig. 4f). An increased hydrogen pressure leads to higher reaction rates over Ru/TiO₂-1; the liquid yield reaches ca. 60% in 6 h (40 bar H₂) and 3 h (50 bar H₂), much faster than the 30 bar experiment. Still, the liquid to gas decomposition is also accelerated (Supplementary Fig. 26, Supplementary Table 12). This competition leads to a maximum liquid yield. The liquid decomposition on the ammonia-treated Ru/TiO₂ samples is less severe, and a maximum is absent at a polymer to catalyst ratio of 20 (Fig. 4a). This maximum is visible at higher catalyst loadings (Fig. 4b, Supplementary Fig. 25) and

shifts to shorter reaction times. The increased H coverage at the same H₂ pressure drives the improved catalyst performance, consistent with the ²H MAS NMR data of the higher content of both Ru–H species and spillover (Fig. 2). We propose that the different nature of chemisorbed hydrogen may be partially responsible for the variation in the liquid yields over different samples. Thus, a simple increase in surface coverage of hydrogen is insufficient to get a similarly high liquid yield over Ru/TiO₂-1 and Ru/TiO₂-8.

Alkane hydrogenolysis invokes (Fig. 5) adsorption to the metal, leading to dehydrogenated intermediates, C–C bond breaking of these intermediates, and final hydrogenation and product release. The first step is usually quasi-equilibrated⁴⁸ due to the lower dehydrogenation barrier than the C–C bond breaking⁴⁹. Experiments in D₂ lead to slower dehydrogenation due to a kinetic isotope effect (KIE) in the dehydrogenation step, while the C–C bond breaking is not strongly affected by the H/D change⁵⁰.

PP hydrogenolysis in D₂ is slower⁶, and the M_w of the liquid is larger, consistent with our data on Ru/TiO₂-1 and Ru/TiO₂-8 (Fig. 4d, e). A prominent shift in M_w is evident over Ru/TiO₂-1 (from 2.67 to 14.12 kDa). Quasi-stationary kinetic analysis with standard transition state theory calculations, based on Fig. 5 (see Supplementary discussion I, Supplementary Fig. 27), shows that increasing the H coverage increases the net hydrogenolysis rate, reduces the KIE, and makes the net reaction rate less sensitive to the H/D exchange. Since Ru/TiO₂-8 has a higher H coverage, the reaction rate is less sensitive to deuteration and correlates with the hydrogenolysis data (Fig. 4a). Over the Ru/TiO₂-8, a high H coverage pushes further C–C bond breaking, leading to consumption of the initial polymer with no solid residue. On Ru/TiO₂-1, the lower H coverage makes

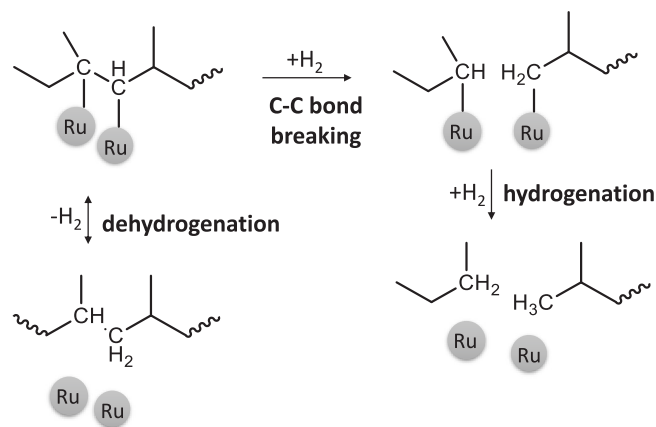


Fig. 5 | Major steps in C-C bond hydrogenolysis of polypropylene. Dehydrogenation happens in both directions, while C-C bond breaking is considered irreversible.

dehydrogenation more kinetically relevant and the initial polymer deconstruction slower.

In PE conversion on Ru/ZrO₂, higher H coverages accelerate the desorption of reaction intermediates, preventing them from over-cracking, and giving higher liquid selectivity over methane at high H₂ pressures. In PP, an increased H coverage boosts all three reaction stages because the PP initial polymer deconstruction is slower than the product desorption. Thus, altering the H coverage primarily alters this reaction step.

Discussion

Ru-based catalysts have demonstrated markedly different performances on various supports, but the reasons have remained elusive. For PE hydrogenolysis over Ru-WO_x/ZrO₂ catalysts¹⁵, a higher H surface coverage shifted the selectivity from terminal to internal C-C bond breaking, reducing methane formation at high hydrogen pressures. Partial reduction of the surface WO_x domains provided extra hydrogen storage, increasing H coverage. Hydrogen availability was hypothesized as important, but the generality of this concept and mechanistic insights leading to catalyst improvement have been lacking.

Here, we tuned the catalyst's electronic properties while holding the Ru particle size and physical characteristics constant by modifying the synthesis using ammonia. Ammonia dehydroxylates the TiO₂ surface reducing the density of Ti-OH groups. This, in turn, increases the Lewis acid strength of Ti⁴⁺ sites, evidenced by FTIR of CO, creating a more intimate contact of Ru and TiO₂ with possible formation of a TiO_x peripheral layer, observed in previous reports²⁴. Upon exposure to H₂, the untreated (Ru/TiO₂-1) sample shows moderate changes. H₂ primarily dissociates and binds to Ru in the atop configuration, confirmed by ²H MAS NMR and DFT. Hydrogen spillover from Ru particles to the support leads to T⁴⁺ + e⁻ → Ti³⁺ reduction with subsequent electron trapping in the bandgap states. New Ti-OH groups form simultaneously, consistent with the classical spillover scheme (Fig. 3a).

For the NH₃ treated samples (Ru/TiO₂-8 and Ru/TiO₂-12), spillover reduces TiO₂ more extensively and forms delocalized e⁻ in the CB in addition to the shallow traps. Ru particles bind more hydrogen, not only covalently (Ru-H_{atop}) but also through weak interactions involving Ru conduction electrons, revealed by ²H MAS NMR. This electron transfer from Ru to H leads to Ru^{δ+}-H⁻ ion pairs as a new H binding mode on Ru. We speculate that TiO₂ CB electrons created by spillover are responsible for activating this new pathway of hydrogen fixation on the Ru/TiO₂ periphery.

Due to the higher H coverage on Ru, these catalysts show higher activity in PP hydrogenolysis leading to higher liquid yields and doing so in a shorter time (6 vs. 16 h). Comparison with previously reported

PP hydrogenolysis results (Supplementary Table 13) shows that Ru/TiO₂-8 provides higher liquid yields at shorter reaction times than Ru/TiO₂-1 and Ru/C. Ru/CeO₂ shows higher liquid yields (83 vs. 74.1%) at higher catalyst loading and longer reaction times, which make a more detailed comparison hard. A similar acceleration is achieved by increasing the hydrogen pressure. High surface H coverage is manifested in a reduced KIE upon H₂/D₂ substitution.

Finally, we proposed a simple way to tune metal-support interactions in Ru/TiO₂ by adding NH₃ as a pH modulator in the Ru deposition step. We demonstrated a boost in hydrogen storage capacity stemming from a pronounced H spillover from Ru to TiO₂. ²H MAS NMR proved to be a sensitive, semi-quantitative tool to study hydrogen chemisorption. Coupled with in situ pretreatment and heating, it can provide direct quantitative monitoring of hydrogen species on metal-metal oxide interfaces. Further improvements to the methodology could expand its scope. Raman, FTIR, and NAP-XPS highlight the enhanced spillover is caused by electrons directly filling the conduction band of TiO₂ compared to the standard localized Ti³⁺ trap sites. This enhances the hydrogen binding capacity for Ru particles due to the relatively weak charge transfer. Technologically, a higher hydrogen coverage increases the liquid yield to ~74% just in 6 h vs. 63% in ~20 h over the conventional catalyst possessing less pronounced MSI. The hydrogen availability drives catalyst improvement and emerges as a general strategy for designing catalysts beyond Ru/TiO₂ and PP hydrogenolysis.

Methods

Catalyst preparation

The Ru/TiO₂ catalysts were prepared by wetness impregnation using a commercially available anatase TiO₂ support (US Research Nanomaterials). Before impregnation, the TiO₂ powder was calcined at 450 °C for 6 h in static air. Ru/TiO₂-1 was prepared by mixing 2.77 g of Ru precursor solution (ruthenium(III) nitrosyl nitrate solution in dilute nitric acid, Sigma-Aldrich) with 1 g of deionized water and then adding it to TiO₂ powder under manual stirring with a glass rod at 70 °C. For Ru/TiO₂-8 and Ru/TiO₂-12, the pH was adjusted accordingly by adding several drops of aqueous NH₃ (25%, Supelco). After impregnation, the catalyst was dried at 100 °C overnight and reduced in H₂ (50% in He) flow in a tubular furnace at 300 °C for 2 h (ramp rate 10 °C/min).

Catalyst characterization

The Ru loading was estimated using X-ray fluorescence (XRF) analysis on a Rigaku Supermini 200 WDXRF in a He atmosphere. XRD (X-ray powder diffraction) patterns were obtained on a Bruker D8 diffractometer with 0.05° 2θ step size using Cu Kα radiation (λ 1.54 Å). Weight vs. temperature curves was recorded on a Discovery TGA instrument in a flow of 5% H₂/He with 10 °C/min ramp from 30 to 600 °C. N₂ sorption isotherms at -196 °C were recorded on a Micromeritics ASAP 2020 instrument. Before measurements, the samples were degassed at 300 °C for 3 h. UV-vis spectra were collected in diffuse-reflectance mode on a spectrometer (JASCO, V-550) with a diffuse-reflectance attachment using an ambient conditions cell with a quartz window and BaSO₄ as a standard. The optical bandgap was estimated using the Tauc plot of (αhν)² vs. hν, where hν is the photon energy in eV, and α is the reflectance. In-house X-ray photoelectron spectra (XPS) were recorded on a Thermo Fisher K-Alpha+ machine with an Al Kα monochromatic source. Before measurements, the samples were reduced in 50% H₂/He flow at 300 °C and then deposited on a Cu foil. For binding energy reference, the C 1s line at 284.6 eV was used. Scanning transmission electron microscopy (STEM) images were acquired on an Aberration Corrected Scanning/Transmission Electron Microscope, JEOL NEOARM TEM/STEM.

Temperature-programmed desorption (TPD) of H₂ was recorded on a Micromeritics Autochem II instrument. Approximately 0.2 g of samples were packed in a U-shaped quartz reactor, heated in 10% H₂/Ar

flow (50 ml/min) to 300 °C with 2 h dwell time. Then samples were cooled to 35 °C in the same 10% H_2 /Ar flow, then purged isothermally for 30 min with pure Ar. Afterward, samples were heated with 10 °C/min ramping rate to 700 °C in Ar flow with an online thermal conductivity detector (TCD) recording of hydrogen desorption. Temperature-programmed reduction (TPR) with H_2 was recorded on the same Autochem II instrument. Samples were pre-reduced in 10% H_2 /Ar (50 ml/min) flow to 300 °C with 2 h dwell time. Then samples were cooled to 35 °C in the same 10% H_2 /Ar flow and then heated with 10 °C/min ramping rate to 700 °C with an online TCD recording of hydrogen consumption. Hydrogen pulse chemisorption at 35 °C was measured on the same instrument. Samples were pretreated in 10% H_2 /Ar flow (50 ml/min) to 300 °C with 2 h dwell time and then for 1 h in pure Ar at the same temperature. Then, the reactor was cooled to 35 °C, and hydrogen was pulsed using 6-port valve with 45 μmol H_2 per pulse, calibrated with the empty reactor.

Fourier transform infrared spectroscopy (FTIR) spectra of adsorbed CO at -196 °C were measured on a Nicolet 8700 spectrometer equipped with liquid nitrogen cooling and an MCT detector. The sample was pressed into a self-supported wafer (64 bar/in²) and loaded into a homemade quartz cell connected to the vacuum line. The sample was pretreated at 300 °C for 1 h in a vacuum (<10⁻⁴ torr). Then the sample was exposed to 1 torr of H_2 gas for 30 min and evacuated for 10 min to reduce Ru. The reduction was repeated four times, followed by a final evacuation for 30 min. Afterward, the sample was cooled to -196 °C and exposed to 1 torr CO to saturate the surface. Then the CO was evacuated till 10⁻³ torr with spectra measured in -0.1 torr increments.

Diffuse-reflectance infrared Fourier transform spectroscopy (DRIFT) spectra, which are more sensitive than FTIR to surface OH groups⁵¹, were recorded on the same spectrometer with a Praying Mantis attachment and in situ Harrick cell. The samples were reduced in 50% H_2 /He flow for 2 h at 300 °C followed by flushing with pure He at 300 °C for 30 min. Then the samples were cooled to 35 °C, and DRIFTS spectra were recorded.

FTIR and Raman spectroscopy of hydrogen spillover

Samples were pressed in self-supporting wafers (64 bar/in²) and placed in a homemade transmission IR cell connected to an atmospheric pressure gas flow manifold. Samples were pre-reduced at 300 °C for 2 h in 100 ml flow of 20% H_2 /He mixture (ramp rate 10 °C/min). Then, the samples were flushed with pure 100 ml/min He flows for 1 h and cooled to treatment temperature (200 or 250 °C). A baseline spectrum was recorded in pure He, and then the gas flow was switched from He to x% H_2 /He with a hydrogen partial pressure ($p(\text{H}_2)$) in the 0.06–0.14 bar range. Spectra were recorded in 10 s increments until complete saturation at a given $p(\text{H}_2)$ and temperature (-15 mins). Then the baseline spectrum was subtracted to highlight the spillover effect.

Raman spectra were measured on a Horiba LabRAM HR evolution spectrometer using 532 nm green laser (5 mW power), $\times 50$ objective, and 1800 g/mm grating. The detector resolution under these conditions is equal to 0.48 cm⁻¹/pixel. In situ measurements were done using a Harrick Raman cell equipped with a quartz window. Samples were pre-reduced at 300 °C for 2 h in 50 ml flow of 20% H_2 /He mixture (ramp rate 10 °C/min). Then, samples were flushed in pure 50 ml/min He flows for 1 h and cooled to treatment temperature (200 or 250 °C). The baseline spectrum was recorded in pure He, and then the gas flow was switched from He to 15% H_2 /He. Spectra were recorded after 10 min stabilization to ensure completion of spillover. Spectra were baseline corrected and fitted using the Lorentzian function in the Omnic software.

²H MAS NMR spectroscopy of chemisorbed deuterium

The sample was packed in ZrO₂ 4 mm standard MAS NMR rotor, loaded in a pyrex tube with a valve, and connected to a vacuum line. Then

it was heated to 120 °C for 1 h to remove moisture and then to 300 °C for 3 h under 10⁻⁴ torr. Then, 1 torr of D₂ gas (99.8%, Cambridge Isotope Laboratories, Inc.) was administered through the vacuum line. After reduction for 30 min, the sample was evacuated for 30 min to remove possible traces of water. The treatment with D₂ at 300 °C was repeated four times. Then the sample was cooled to room temperature under 1 torr D₂ and transferred to a glove box without exposure to air. In nitrogen, the glove box rotor was removed from the tube and sealed. To test the stability of chemisorbed deuterium, in an experiment, the sample was degassed at 100 °C for 30 min at 10⁻⁴ torr and only then sealed.

²H MAS NMR spectra were acquired on an 11.7 T Bruker Avance III NMR spectrometer with a 4 mm HX probe at a ²H frequency of 76.77 MHz at magic angle spinning speeds of 4 and 10 kHz. The samples were maintained at room temperature with sample heating due to magic angle spinning taken into account. Data were acquired using a 180°- τ -90° pulse sequence with an interpulse delay of 10 ms to reduce baseline distortions, with a 90° pulse length of 4.25 μs . 16,384–20,480 scans were collected per sample with a pulse delay of 4 s. Spectra were referenced externally to D₂O at 4.7 ppm.

Spectra were modeled and fitted using the ssNake software⁵², and three component refinement of the experimental spectra was performed to estimate the key EFG parameters.

Near ambient pressure X-ray photoelectron spectroscopy (NAP-XPS)

The NAP-XPS spectra were collected under UHV (base pressure of 10⁻⁹ mbar) using a SPECS electron spectrometer equipped with PHOIBOS 100 hemispherical energy analyzer and a monochromatic Al K α X-ray source (1486.7 eV). Spectra were referenced to C1s line at 284.6 eV and fitted using Thermo Avantage software. The samples were pressed on a Cu piece and mounted on a stainless-steel flag-type holder with a K-type thermocouple allowing for in situ temperature readings. After loading the sample in XPS analysis chamber, it was heated to 300 °C and kept at that temperature for 30 min (ramp rate 10 °C/min). Then 1 mbar hydrogen was dosed for in situ reductions at 300 °C for 40 min. Then hydrogen was evacuated, and the sample was annealed at 300 °C in UHV for 10 min to remove chemisorbed hydrogen. Afterward, the sample was cooled to 200 °C, and initial spectra in UHV were recorded. Then the sample was exposed to 1 mbar hydrogen for 15 min at the same temperature and new spectra were measured. Additional reference spectra were recorded also at 35 °C in UHV.

Reaction tests

Isotactic polypropylene (PP, M_w -250,000, M_n -67,000) was purchased from Sigma-Aldrich. An amount of freshly reduced catalyst (0.1 or 0.05 g) was mechanically mixed with 2.0 g of PP using a vortex mixer. The mixture was then transferred into a borosilicate liner of a 50 mL stainless-steel Parr reactor with a 0.7 mL stir bar. The mass ratio of polymer to catalyst was 20 or 40, corresponding to the catalyst loading of 0.1 or 0.05 g. The Parr reactor was sealed and purged six times with pure H_2 at 50 bar, charged to 30 bar, and then heated to 250 °C (ramping rate 10 °C/min) using a band heater (Omega Eng.). Stirring was initiated after the temperature reached 160 \pm 5 °C to first melt the polymer. The stirring speed was set at 300 rpm; additional experiments showed similar product yields and molecular weight distributions at 400 and 500 rpm but nearly no reactivity without stirring. Reactions were maintained for specified time intervals and then quickly quenched in an ice bath. For H_2 pressure variation experiments, the hydrogen pressure was 20, 40, and 50 bar.

Product analysis

After the temperature dropped below 10 °C, the gas from the reactor's headspace was transferred to a 1 L Tedlar gas sampling bag for analysis.

Then the reactor was opened, and the liquid and solid residue were mixed with 20 mL of CH_2Cl_2 , used as a solvent. This slurry was filtered (Whatman, 100 μm), and the solid residue was dried at room temperature overnight with complete evaporation of all CH_2Cl_2 . The solvent was removed from the liquid fraction using a rotary evaporator. The solid and liquid fraction yields were quantified gravimetrically. A GC with an FID detector (Agilent 7890 Series, HP-volatile column) was used for gas analysis. The concentration of hydrocarbons in the gas sample was calculated using a standard C_1 – C_4 calibration mixture. The absolute amount of hydrocarbons in the gas was calculated using the ideal gas law.

An overall balance was calculated according to Eq. (1):

$$\text{Material balance} = \frac{m_L + m_s + m_g}{m_{\text{initial}}} \cdot 100\% \quad (1)$$

where $m_L, m_s, m_g, m_{\text{initial}}$ are the mass of liquid, gas, solid, and initial polymer, respectively. The yield of the i -th group of products was calculated according to Eq. (2):

$$Y_i = \frac{m_i}{m_{\text{initial}}} \cdot 100\% \quad (2)$$

where m_i is the mass of the i th group of products (liquid, gas, or solid).

Liquid products were analyzed using gel permeation chromatography (GPC) using Styragel HR 4, HR 3, and HR 0.5 columns (dimensions 4.6×300 mm) connected in tandem using THF as solvent (0.3 ml/min flow rate) and a Waters 2414 refractive index detector (RID). The retention time was calibrated using Polystyrene Standards Kit (Waters, WAT058931).

Density functional theory (DFT) calculations

The TiO_2 support was modeled as an anatase structure with the (101) facet exposed. The supported Ru was modeled as a Ru-12 cluster on the TiO_2 surface. DFT calculations were performed using the Vienna Ab initio Simulation Package (VASP) package⁵³. The RPBE potential was used in conjunction with the D3 correction⁵⁴. The energy cutoff was set as 520 eV, and the electron smearing factor was set as 0.1 eV. Electronic structures were convergence until 10^{-6} eV, and ionic steps were iteratively taken until the force fell below 0.05 eV/Å. The Electric Field Gradient (EFG) was calculated using the VASP internal functions. Nuclear quadrupole moments were adapted accordingly⁵⁵.

Data availability

All data generated or analyzed during this study are included in this published article (and its supplementary information file).

References

- Silva, A. L. P. et al. Increased plastic pollution due to COVID-19 pandemic: challenges and recommendations. *Chem. Eng. J.* **405**, 126683 (2021).
- Zheng, J. & Suh, S. Strategies to reduce the global carbon footprint of plastics. *Nat. Clim. Change* **9**, 374–378 (2019).
- Vanapalli, K. R. et al. Challenges and strategies for effective plastic waste management during and post COVID-19 pandemic. *Sci. Total Environ.* **750**, 141514 (2021).
- Moncrief, L. J., Maggie, G., Bryan, B., Eric, N. A. & Elizabeth, H. J. *Articles of reclaimed polypropylene compositions*. USA patent (2016).
- Kots, P. A., Vance, B. C. & Vlachos, D. G. Polyolefin plastic waste hydroconversion to fuels, lubricants, and waxes: a comparative study. *React. Chem. Eng.* **7**, 41–54 (2022).
- Kots, P. A. et al. Polypropylene plastic waste conversion to lubricants over Ru/ TiO_2 catalysts. *ACS Catal.* **11**, 8104–8115 (2021).
- Jaydev, S. D., Martín, A. J. & Pérez-Ramírez, J. Direct conversion of polypropylene into liquid hydrocarbons on carbon-supported platinum catalysts. *ChemSusChem* **14**, 5179–5185 (2021).
- Celik, G. et al. Upcycling single-use polyethylene into high-quality liquid products. *ACS Cent. Sci.* **5**, 1795–1803 (2019).
- Zhang, F. et al. Polyethylene upcycling to long-chain alkylaromatics by tandem hydrogenolysis/aromatization. *Science* **370**, 437–441 (2020).
- Rorrer, J. E., Beckham, G. T. & Román-Leshkov, Y. Conversion of polyolefin waste to liquid alkanes with Ru-based catalysts under mild conditions. *JACS Au*, **1**, 8–12 (2020).
- Nakaji, Y. et al. Low-temperature catalytic upgrading of waste polyolefinic plastics into liquid fuels and waxes. *Appl. Cat. B Environ.* **285**, 119805 (2021).
- Rorrer, J. E., Troyano-Valls, C., Beckham, G. T. & Román-Leshkov, Y. Hydrogenolysis of polypropylene and mixed polyolefin plastic waste over Ru/C to produce liquid alkanes. *ACS Sustain. Chem. Eng.* **9**, 11661–11666 (2021).
- Jia, C. et al. Deconstruction of high-density polyethylene into liquid hydrocarbon fuels and lubricants by hydrogenolysis over Ru catalyst. *Chem. Catal.* **1**, 437–455 (2021).
- Chen, L. et al. Effect of reaction conditions on the hydrogenolysis of polypropylene and polyethylene into gas and liquid alkanes. *React. Chem. Eng.*, **7**, 844–854 (2022).
- Wang, C. et al. Polyethylene hydrogenolysis at mild conditions over ruthenium on tungstated zirconia. *JACS Au* **1**, 1422–1434 (2021).
- Tauster, S., Fung, S. & Garten, R. L. Strong metal-support interactions. Group 8 noble metals supported on titanium dioxide. *J. Am. Chem. Soc.* **100**, 170–175 (1978).
- Zhou, J. et al. Interfacial compatibility critically controls Ru/ TiO_2 metal-support interaction modes in CO_2 hydrogenation. *Nat. Commun.* **13**, 1–10 (2022).
- Lin, F. et al. Single-facet dominant anatase TiO_2 (101) and (001) model catalysts to elucidate the active sites for alkanol dehydration. *ACS Catal.* **10**, 4268–4279 (2020).
- Fàbrega, C. et al. Tuning the fermi level and the kinetics of surface states of TiO_2 nanorods by means of ammonia treatments. *J. Phys. Chem. C.* **117**, 20517–20524 (2013).
- Román, E. L., de Segovia, J., Kurtz, R. L., Stockbauer, R. & Madey, T. E. UPS synchrotron radiation studies of NH_3 adsorption on TiO_2 (110). *Surf. Sci.* **273**, 40–46 (1992).
- Hadjivanov, K., Lamotte, J. & Lavalley, J.-C. FTIR study of low-temperature CO adsorption on pure and ammonia-precured TiO_2 (anatase). *Langmuir* **13**, 3374–3381 (1997).
- Panayotov, D. A. et al. Effect of methanol on the Lewis acidity of rutile TiO_2 nanoparticles probed through vibrational spectroscopy of coadsorbed CO. *Langmuir* **26**, 8106–8112 (2010).
- Hadjivanov, K. et al. FTIR study of CO interaction with Ru/ TiO_2 catalysts. *J. Catal.* **176**, 415–425 (1998).
- Zhang, Y. et al. Tuning reactivity of Fischer–Tropsch synthesis by regulating TiO_x overlayer over Ru/ TiO_2 nanocatalysts. *Nat. Commun.* **11**, 1–8 (2020).
- Feulner, P. & Menzel, D. The adsorption of hydrogen on ruthenium (001): adsorption states, dipole moments and kinetics of adsorption and desorption. *Surf. Sci.* **154**, 465–488 (1985).
- Zhan, Y., Zhou, C., Jin, F., Chen, C. & Jiang, L. Ru/ TiO_2 catalyst for selective hydrogenation of benzene: Effect of surface hydroxyl groups and spillover hydrogen. *Appl. Surf. Sci.* **525**, 146627 (2020).
- Gutmann, T. et al. Hydrido-ruthenium cluster complexes as models for reactive surface hydrogen species of ruthenium nanoparticles. solid-state ^2H NMR and quantum chemical calculations. *J. Am. Chem. Soc.* **132**, 11759–11767 (2010).
- Walaszek, B. et al. ^2H -solid-state-NMR study of hydrogen adsorbed on catalytically active ruthenium coated mesoporous silica materials. *Solid State Nucl. Magn. Reson.* **35**, 164–171 (2009).

29. Prins, R. Hydrogen spillover. *Facts fiction. Chem. Rev.* **112**, 2714–2738 (2012).
30. Chen, H.-Y. T., Tosoni, S. & Pacchioni, G. Hydrogen adsorption, dissociation, and spillover on Ru₁₀ clusters supported on anatase TiO₂ and tetragonal ZrO₂ (101) surfaces. *ACS Catal.* **5**, 5486–5495 (2015).
31. Engelke, F., Bhatia, S., King, T. S. & Pruski, M. Dynamics of hydrogen at the surface of supported ruthenium. *Phys. Rev. B* **49**, 2730 (1994).
32. Komaya, T. et al. The influence of metal-support interactions on the accurate determination of Ru dispersion for Ru/TiO₂. *J. Catal.* **149**, 142–148 (1994).
33. Yesinowski, J. P. et al. Distributions of conduction electrons as manifested in MAS NMR of gallium nitride. *J. Am. Chem. Soc.* **128**, 4952–4953 (2006).
34. Mehta, M. et al. Hydrogen treated anatase TiO₂: a new experimental approach and further insights from theory. *J. Mater. Chem. A* **4**, 2670–2681 (2016).
35. Sinhamahapatra, A., Lee, H.-Y., Shen, S., Mao, S. S. & Yu, J.-S. H-doped TiO_{2-x} prepared with MgH₂ for highly efficient solar-driven hydrogen production. *Appl. Cat. B Environ.* **237**, 613–621 (2018).
36. Komaya, T. et al. Effects of sodium on the structure and Fischer-Tropsch synthesis activity of Ru/TiO₂. *J. Catal.* **152**, 350–359 (1995).
37. Di Valentin, C., Pacchioni, G. & Selloni, A. Reduced and n-type doped TiO₂: nature of Ti³⁺ species. *J. Phys. Chem. C.* **113**, 20543–20552 (2009).
38. Panayotov, D. et al. Hydrogen spillover on Rh/TiO₂: the FTIR study of donated electrons, co-adsorbed CO and H/D exchange. *Phys. Chem. Chem. Phys.* **17**, 20563–20573 (2015).
39. Mahdavi-Shakib, A., Rich, L. C., Whittaker, T. N. & Chandler, B. D. Hydrogen adsorption at the Au/TiO₂ interface: quantitative determination and spectroscopic signature of the reactive interface hydroxyl groups at the active site. *ACS Catal.* **11**, 15194–15202 (2021).
40. Panayotov, D. A., Burrows, S. P., Yates, J. T. Jr. & Morris, J. R. Mechanistic studies of hydrogen dissociation and spillover on Au/TiO₂: IR spectroscopy of coadsorbed CO and H-donated electrons. *J. Phys. Chem. C.* **115**, 22400–22408 (2011).
41. Panayotov, D. A. & Yates, J. T. Jr. Depletion of conduction band electrons in TiO₂ by water chemisorption—IR spectroscopic studies of the independence of Ti–OH frequencies on electron concentration. *Chem. Phys. Lett.* **410**, 11–17 (2005).
42. Mazzolini, P. et al. Vibrational–electrical properties relationship in donor-doped TiO₂ by Raman spectroscopy. *J. Phys. Chem. C.* **120**, 18878–18886 (2016).
43. Abdel-Mageed, A. M. et al. Steering the selectivity in CO₂ reduction on highly active Ru/TiO₂ catalysts: Support particle size effects. *J. Catal.* **401**, 160–173 (2021).
44. Elmasides, C., Kondarides, D., Grünert, W. & Verykios, X. XPS and FTIR study of Ru/Al₂O₃ and Ru/TiO₂ catalysts: reduction characteristics and interaction with a methane–oxygen mixture. *J. Phys. Chem. B* **103**, 5227–5239 (1999).
45. Whittaker, T. et al. H₂ oxidation over supported Au nanoparticle catalysts: evidence for heterolytic H₂ activation at the metal–support interface. *J. Am. Chem. Soc.* **140**, 16469–16487 (2018).
46. Li, X. et al. Controlling CO₂ hydrogenation selectivity by metal-supported electron transfer. *Angew. Chem. Int. Ed.* **59**, 19983–19989 (2020).
47. Verdinelli, V., Juan, A. & German, E. Ruthenium decorated single walled carbon nanotube for molecular hydrogen storage: A first-principle study. *Int. J. Hydrog. Energy* **44**, 8376–8383 (2019).
48. Flaherty, D. W. & Iglesia, E. Transition-state enthalpy and entropy effects on reactivity and selectivity in hydrogenolysis of n-alkanes. *J. Am. Chem. Soc.* **135**, 18586–18599 (2013).
49. Zaera, F. An organometallic guide to the chemistry of hydrocarbon moieties on transition metal surfaces. *Chem. Rev.* **95**, 2651–2693 (1995).
50. Shi, H., Gutierrez, O. Y., Zheng, A., Haller, G. L. & Lercher, J. A. Mechanistic pathways for methylcyclohexane hydrogenolysis over supported Ir catalysts. *J. Phys. Chem. C.* **118**, 20948–20958 (2014).
51. Halasz, I., Moden, B., Petushkov, A., Liang, J.-J. & Agarwal, M. Delicate distinction between OH groups on proton-exchanged H-chabazite and H-SAPO-34 molecular sieves. *J. Phys. Chem. C.* **119**, 24046–24055 (2015).
52. Van Meerten, S., Franssen, W. & Kentgens, A. ssNake: a cross-platform open-source NMR data processing and fitting application. *J. Magn. Reson.* **301**, 56–66 (2019).
53. Kresse, G. & Hafner, J. Ab initio molecular dynamics for open-shell transition metals. *Phys. Rev. B* **48**, 13115 (1993).
54. Grimme, S., Ehrlich, S. & Goerigk, L. Effect of the damping function in dispersion corrected density functional theory. *J. Comput. Chem.* **32**, 1456–1465 (2011).
55. Pyykkö, P. Year-2008 nuclear quadrupole moments. *Mol. Phys.* **106**, 1965–1974 (2008).

Acknowledgements

We thank to Dr. Stavros Caratzoulas for valuable discussions. This work was financially supported by the Center for Plastics Innovation (CPI), an Energy Frontier Research Center funded by the US Department of Energy, Office of Science, Office of Basic Energy Sciences, award number DE-SC0021166. This research used instruments in the Advanced Materials Characterization Lab (AMCL) at the University of Delaware. MAS NMR measurements were made possible by the Delaware COBRE program, supported by a grant from the National Institute of General Medical Sciences—NIGMS (5 P30 GM110758-02) from the National Institutes of Health. STEM was performed at the Singh Center for Nanotechnology at the University of Pennsylvania, supported by the National Science Foundation (NSF) National Nanotechnology Coordinated Infrastructure Program grant NNCI-1542153. Additional support to the Nanoscale Characterization Facility at the Singh Center has been provided by the Laboratory for Research on the Structure of Matter (MRSEC) supported by the National Science Foundation (DMR-1720530). This research used beamline 7-BM (QAS) of the National Synchrotron Light Source II, a U.S. DOE Office of Science User Facility operated for the DOE Office of Science by Brookhaven National Laboratory under Contract No. DE-SC0012704. Beamline operations were supported in part by the Synchrotron Catalysis Consortium (U.S. DOE, Office of Basic Energy Sciences, Grant No. DE-SC0012335). This research used resources of the Center for Functional Nanomaterials (CFN), which is a U.S. Department of Energy Office of Science User Facility, at Brookhaven National Laboratory under Contract No. DE-SC0012704.

Author contributions

P.A.K. conceived the idea, designed the project, and carried out the experiments. T.X. performed DFT calculations and the associated analysis. B.C.V. and C.W. carried out some experiments and contributed to the discussions. C.M.Q. measured and analyzed the MAS NMR spectra. M.D.M. and J.A.B. performed and analyzed the NAP-XPS data. P.K. and E.A.S. took and analyzed the STEM images. N.S.M., L.M., and S.N.E. performed in situ XAS data collection and analysis. D.G.V. supervised the project. P.A.K. and D.G.V. wrote the manuscript, and all authors discussed the results and assisted the manuscript preparation.

Competing interests

D.G.V., P.A.K., B.C.V., and C.W. are authors of a patent application. The remaining authors declare no competing interests.

Additional information

Supplementary information The online version contains supplementary material available at <https://doi.org/10.1038/s41467-022-32934-5>.

Correspondence and requests for materials should be addressed to Dionisios G. Vlachos.

Peer review information *Nature Communications* thanks Masazumi Tamura and the other, anonymous, reviewers for their contribution to the peer review of this work.

Reprints and permission information is available at <http://www.nature.com/reprints>

Publisher's note Springer Nature remains neutral with regard to jurisdictional claims in published maps and institutional affiliations.

Open Access This article is licensed under a Creative Commons Attribution 4.0 International License, which permits use, sharing, adaptation, distribution and reproduction in any medium or format, as long as you give appropriate credit to the original author(s) and the source, provide a link to the Creative Commons license, and indicate if changes were made. The images or other third party material in this article are included in the article's Creative Commons license, unless indicated otherwise in a credit line to the material. If material is not included in the article's Creative Commons license and your intended use is not permitted by statutory regulation or exceeds the permitted use, you will need to obtain permission directly from the copyright holder. To view a copy of this license, visit <http://creativecommons.org/licenses/by/4.0/>.

© The Author(s) 2022